REVISTAS CIENTÍFICAS INDEXADAS
BISTUA
FACULTAD DE CIENCIAS BÁSICAS - UNIVERSIDAD DE PAMPLONA
fcb Facultad de Ciencias Básicas Universidad de Pamplona

BISTUA ***Rev. FCB, Volumen 23 (2) (2025). Pamplona-Colombia.***
https://doi.org/10.24054/bistua.v23i2.3672

Nucleation and growth history of garnet in metamorphic rocks: 2D and 3D petrological insights

Historia de nucleación y crecimiento del granate en rocas metamórficas: Perspectivas petrológicas en 2D y 3D

Leydy Mariana Hernández-Marín [a]; Carlos Alberto Chacón-Ávila [b]; Carlos Alberto Ríos-Reyes [b]; Oscar Mauricio Castellanos-Alarcón[a]

[a] *Universidad de Pamplona, Programa de Geología, Villa del Rosario, Colombia*
[b] *Universidad Industrial de Santander, Escuela de Geología, Bucaramanga, Colombia*

Correspondence: *oscarmca@yahoo.es*

Submitted*: Mayo 31, 2025.* ***Accepted****: Diciembre 30, 2025.*

Abstract

This study investigates garnet nucleation and growth in metamorphic rocks through integrated controlled serial sectioning, high-resolution backscattered electron (BSE) imaging, and three-dimensional reconstruction. Implementation of a systematic material removal protocol significantly enhanced surface reproducibility and analytical consistency relative to conventional manual preparation methods. A dataset of 2,100 BSE images enabled the generation of high-resolution mosaics via automated image stitching. Digital processing and algorithmic segmentation allowed quantitative characterization of particle size distributions (PSD) across 50 consecutive layers. The resulting Gaussian PSD indicates spatial and temporal variability in nucleation rates and growth regimes, providing kinetic constraints on crystallization processes within the Arquía Complex. The integration of advanced imaging and computational modeling establishes a quantitative petro-textural framework for 2D and 3D analysis of metamorphic rocks, enabling rigorous assessment of grain size, morphology, orientation proxies, and spatial distribution of mineral phases, pores, and fractures. These parameters are critical for interpreting metamorphic reactions and reconstructing tectonometamorphic evolution. Our findings provide new quantitative constraints on garnet crystallization mechanisms and their role in regional metamorphic development.

Keywords**:** crystal size distribution; garnet; serial sectioning; nucleation; growth; Arquía Complex.

Resumen

Este estudio aborda la nucleación y el crecimiento del granate en rocas metamórficas mediante la integración de corte en serie controlado, imagenología de electrones retrodispersados (BSE) de alta resolución y reconstrucción tridimensional. La implementación de un protocolo sistemático de remoción de material mejoró la reproducibilidad superficial y la consistencia analítica frente a métodos manuales convencionales. Un total de 2.100 imágenes BSE permitió generar mosaicos de alta resolución mediante ensamblaje automatizado. El procesamiento digital y la segmentación algorítmica posibilitaron la cuantificación de las distribuciones de tamaño de partícula (PSD) en 50 capas consecutivas. La distribución gaussiana obtenida sugiere variabilidad espacio-temporal en las tasas de nucleación y en los regímenes de crecimiento, aportando restricciones cinéticas a los procesos de cristalización en el Complejo de Arquía. La integración de imagenología avanzada y modelado computacional establece un marco petro-textural cuantitativo para el análisis 2D y 3D de rocas metamórficas, permitiendo caracterizar tamaño, morfología, orientación y distribución espacial de fases minerales, poros y fracturas. Estos parámetros son esenciales para interpretar reacciones metamórficas y reconstruir trayectorias tectonometamórficas. Los resultados proporcionan nuevas restricciones cuantitativas sobre los mecanismos de cristalización del granate y su papel en la evolución metamórfica regional.

Palabras clave**:** distribución del tamaño de cristales; granate; corte en serie; nucleación; crecimiento; Complejo de Arquía.

1. Introduction

Recent advancements in imaging technologies, along with innovative computer processing and modeling techniques, have transformed the landscape of petrology, enabling detailed analysis of rock textures at both two-dimensional (2D) and three-dimensional (3D) scales. These advancements are crucial for understanding the geological history of metamorphic rocks, as mineral textures provide essential information about the processes that shaped them over time. Understanding the intricate texture of metamorphic rocks is important for unraveling the geological processes that have

transformed them. Key parameters such as size, shape, orientation, and spatial distribution of mineral phases, pores, and fractures can now be quantified with precision [1-11]. However, despite these advancements, significant challenges remain in accurately capturing the 3D architecture of metamorphic minerals, particularly garnet, which is fundamental for interpreting metamorphic conditions and processes. The study of garnet's nucleation and growth within metamorphic rocks is essential for understanding the evolution of these geological formations. Garnet porphyroblasts can provide valuable insights into the thermal and pressure conditions experienced during metamorphism. Despite previous research utilizing various imaging techniques, there is an ongoing need for more systematic and refined approaches that integrate both 2D and 3D analyses to fully capture the complexities of mineral development in metamorphic settings. This study specifically focuses on the 3D reconstruction of a garnet-bearing rock sample from the Arquía Complex in the Colombian Andes. By employing a combination of serial sectioning and backscattered electron (BSE) imaging, we aim to produce a high-resolution dataset that elucidates the nucleation and growth processes of garnet under varying metamorphic conditions [12]. The particle size distribution (PSD) of garnet serves as a critical parameter in understanding crystallization kinetics, providing insights into the timing and conditions of mineral formation [13-14]. In this con-text, our research addresses a significant gap in the existing literature by proposing a robust and detailed methodology for specimen preparation and imaging, with an emphasis on precision and reproducibility. Our protocols include rigorous procedures for serial sectioning, image acquisition, and processing, allowing for the creation of comprehensive 3D models of garnet morphology. By leveraging advanced software tools, we transform our dataset into visually and quantitatively rich representations that enable detailed exploration of garnet's textural evolution. In addition to these methods, Furthermore, recent advancements in crystallographic studies, such as the integration of infrared digital holography, offer a promising complementary technique [15]. This method can dynamically observe the crystallization process and capture phase attributes of minerals in real time, providing a more comprehensive understanding of garnet's microstructure and deformation mechanisms. Combining this with BSE imaging could offer a more holistic view of garnet's crystallization behavior under varying metamorphic conditions. In the following sections, we first detail the experimental procedures used, including specimen preparation, the detailed serial sectioning process, and the methods employed for image acquisition and analysis. Next, we present our results, with a particular focus on the PSD of garnet and its implications for understanding nucleation and growth dynamics. Finally, we discuss the significance of our findings in the broader context of metamorphic petrology, offering new perspectives on garnet's textural evolution and its role in interpreting metamorphic processes. This study represents a significant advancement in the field of petrology by providing new insights into the complex processes governing garnet nucleation and growth. By employing a multidimensional analytical framework that integrates both 2D and 3D analysis techniques, we aim to set a precedent for future research in this domain and contribute to a deeper understanding of metamorphic rocks and their formation histories [6,8,16].

2. Experimental Procedure

The experimental procedure for the preparation of a single rock specimen, including serial sectioning, image acquisition, and 3D reconstruction, is illustrated in Fig. 1. The garnet-bearing rock sample was collected from the Arquía Complex on the western flank of the Central Cordillera, selecting an outcrop with a high concentration of garnet within metabasic lithologies (garnet-bearing amphibolites). Structural conditions, outcropping lithologies, and mineralogical features were considered to ensure the sample was representative of the typical high-pressure and high-temperature metamorphic rocks of the complex, formed through regional metamorphism of basaltic protoliths under amphibolite facies conditions, producing garnet, amphibole, and plagioclase.

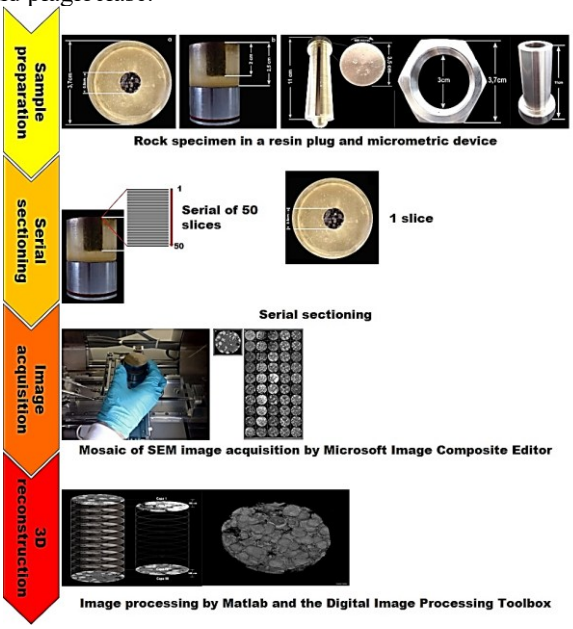

Figure 1. Experimental set up for rock specimen preparation, serial sectioning, image acquisition and 3D reconstruction.

A microplug of the selected rock (8 mm in diameter and 15 mm in length) was embedded in a resin plug (30 mm in diameter and 20 mm in length) and secured to a stainless-steel holder that allows controlled displacement along a stainless-steel apparatus equipped with a micrometric screw (110 mm length, 35 mm thread diameter, 0.5 mm pitch), a 30 mm diameter locknut, and an assembly screw of the same dimensions (Fig. 1a). The serial sectioning of the rock specimen (Fig. 1b) was carried out at intervals of approximately 0.01 mm (100 μm), ensuring precise control over section spacing. Following this, the specimen underwent

mechanical polishing using a BUEHLER MetaServ 3000 Variable Speed Grinder Polisher, using grinding papers of grades 220, 400, 600, and 1200, followed by an alumina solution to create smooth surfaces suitable for scanning electron microscopy (SEM) analysis. After being mounted on an aluminum pin and coated with a thin layer of carbon, the specimen was analyzed using BSE imaging in a FEI FEG ESEM QUANTA 650. The polished surfaces were sectioned into fifty parallel layers, each producing 42 BSE images. These images were then processed using Microsoft Image Composite Editor software [17] to create a mosaic representation (Fig. 1c). For 3D reconstruction, an algorithm was developed for the 2D processing of the garnets present in the sample, using Matlab and the Digital Image Processing Toolbox (Fig. 1d).

3. Results

3.1. Serial sectioning thickness

During serial sectioning, precise control of material removal is achieved by regulating equipment speed, load, and processing time (Fig. 2), improving upon earlier manual techniques that commonly introduced polishing errors [18–19]. To overcome these limitations, previous studies developed mathematical models and control strategies to maintain constant pressure and predict surface residual errors [19–20]. Compared with these approaches, our results show enhanced precision, efficiency, and reproducibility in the polishing process. Serial sectioning generates successive parallel slices, making section thickness a critical parameter. An optimal thickness, typically between 50 and 100 µm, minimizes gaps during 3D reconstruction while reducing the total number of sections required. Thinner sections increase resolution but also the number of slices and potential reconstruction noise, whereas thicker sections reduce acquisition time but may obscure fine structural details. In this study, a thickness of 100 µm was selected as a balance between resolution and efficiency. Section thickness also influences PSD analysis, as thicker slices may average fine features and affect particle size interpretation. Future studies should carefully select the cutting plane to reduce ambiguities caused by surfaces nearly parallel to slice planes and improve reconstruction accuracy. Mechanical polishing presents limitations compared to techniques such as FIB-SEM, particularly in the number of sections produced. Here, only 50 slices were prepared due to time constraints, whereas FIB-SEM can generate up to 500 slices. However, mechanical polishing is faster (1–4 h per slide), while FIB-SEM requires longer processing times (30 min to several hours per slide). Mechanical polishing is therefore suitable for rapid surface preparation, whereas FIB-SEM is preferable for micro- to nano-scale resolution despite longer processing times. Polishing efficiency is further influenced by material hardness, mineral composition, sample size, abrasive type, rotational speed, applied pressure, and the use of multiple polishing stages, which together control surface quality and preparation time.

Figure 2. Serial sections of garnet-bearing metamorphic rock.

3.2. Image acquisition

For the analysis of the polished rock surface, 42 BSE images of 1200 pixels each were acquired per section (Fig. 3), resulting in a dataset of 2100 images across the 50 analyzed layers. The initial vertical spacing between layers was 500 µm and was later refined to 250 µm to improve depth resolution. This systematic acquisition strategy ensured comprehensive coverage of the sample and enhanced the characterization of its internal structure. In contrast, recent SEM image acquisition studies emphasize advanced approaches to improve resolution and spatial coverage, including automated acquisition and image stitching techniques [21–23], which generate large-format, high-resolution datasets using multiple detector types [22,24], reflecting a shift toward more sophisticated and data-intensive imaging methodologies.

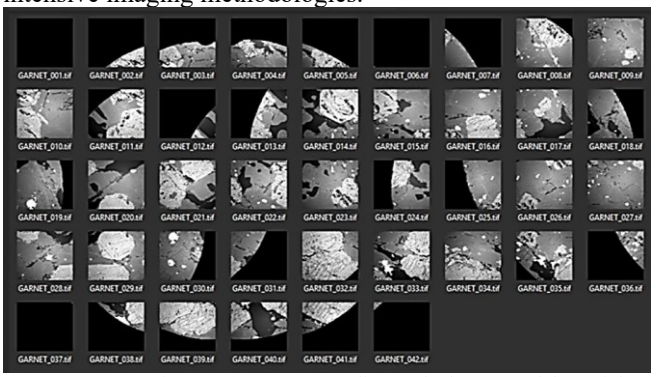

Figure 3. BSE images (42) corresponding to the layer 50 of the serial sectioning.

3.3. Image stitching

To generate overlapping BSE images and produce a high-resolution mosaic (5300 pixels), Microsoft Image Composite Editor (ICE) v1.4.4.0 for Windows was used [17]. This image stitching technique combines individual images into a seamless mosaic, resulting in stitched images measuring 1.65 mm × 1.24 mm, saved in TIFF format for detailed two-dimensional visualization (Fig. 4), with additional examples shown in Fig. 5. Microsoft ICE, developed by the Microsoft Research Interactive Visual Media Group, has been successfully applied in microscopy image integration for surface analysis [25–26] and is freely available for non-

commercial use, although it does not support stitching images from entirely different scenes. While the present study focuses on 2D image mosaics, extending the analysis into 3D would require transforming stacked 2D images into voxel-based datasets using established reconstruction approaches such as image segmentation [27–30], multi-view stereo (MVS) methods [31–32], or depth map fusion techniques [33]. These methods enable the generation of 3D models from overlapping 2D images, allowing detailed analysis of internal rock features, including mineral distribution, porosity, microstructural variations, surface roughness, and volumetric characteristics [34–36]. Although beyond the scope of this study, integrating 3D reconstruction algorithms with the image stitching workflow represents a promising direction for future work, enabling comprehensive 2D and 3D analyses of rock microstructures.

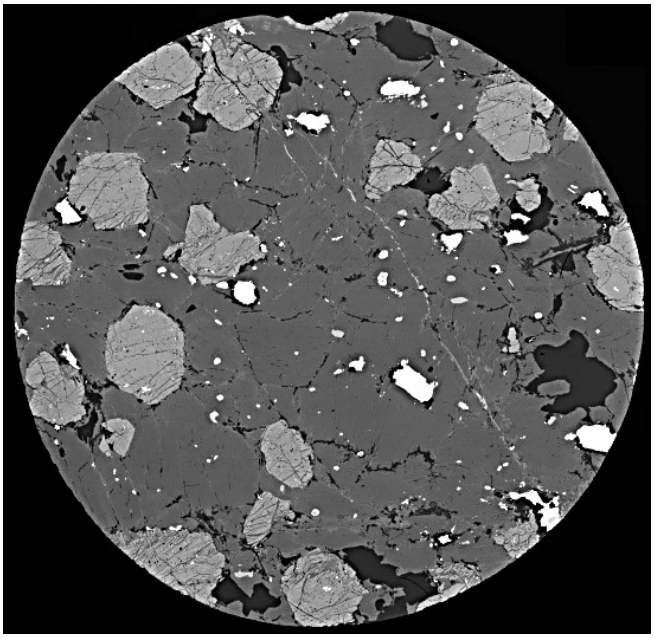

Figure 4. A high-resolution mosaic of BSE images corresponding to the layer 50.

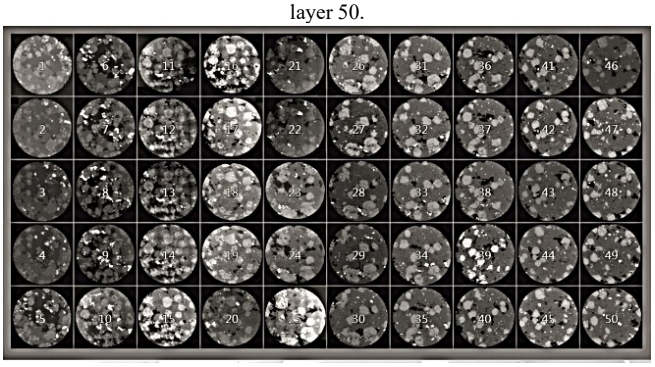

Figure 5. High-resolution mosaics of BSE images corresponding to the analyzed layers of the gar-net-bearing metamorphic rock.

3.4. Data storage and image digitization

The stitched image mosaics were stored for subsequent automated digitization using software based on image resolution and gray-level threshold parameters. Three-dimensional visualization of rock textures and microstructures was achieved by stacking 2D serial sections through computer-based reconstruction algorithms [37]. The achievable resolution is constrained by the spacing between sections, which can be reduced to a few microns using serial sectioning jigs [3]. For isotropic voxel resolution, section spacing was matched to the image resolution [38], allowing comprehensive analysis of the rock volume. In coarse-grained samples, lower resolution in the grinding direction can be applied to increase sampled volume and reduce dataset size [39]. Although serial sectioning by grinding and polishing is time-consuming, it can produce results comparable to low-resolution X-ray tomography [3]. BSE images were used to capture mineralogical variations across layers, with garnet isolated in each section using the Matlab Image Processing Toolbox. The 2D processing workflow consisted of image alignment, segmentation, and noise removal with true-color parameterization. Recent advances in 3D voxel reconstruction include algorithms such as back projection, filtered back projection, inverse Radon transform, marching cubes, ray casting, interpolation, and view-based reconstruction, which have been evaluated for accuracy, computational efficiency, and dimensional integrity [40–45]. In geological applications, these methods are widely used in CT and μCT to visualize porosity, fractures, and internal structures. In this study, a Matlab-based voxel transformation approach was applied to ensure accurate alignment and scaling in all three dimensions, minimizing distortions reported in lower-resolution reconstructions. This approach aligns with current trends in 3D reconstruction research and highlights potential improvements in volumetric data processing for geological specimens.

3.4.1. Alignment of the stitched images

Image registration is a fundamental process for aligning images from multiple datasets and constitutes the basis for advanced image analysis, enabling the generation of composite views, improvement of signal-to-noise ratios, and extraction of information not evident in single images [46]. According to Patil *et al*. [47], image registration comprises four core components: (1) the feature set, which includes image characteristics such as intensity, contours, and texture; (2) the similarity measure, which quantifies the correspondence between image features; (3) the search set, consisting of possible transformations such as translation, rotation, and scaling; and (4) the search strategy, which defines the algorithm used to select optimal transformations. Beyond 2D alignment, image registration is closely linked to voxel transformation, a key step in converting 2D image stacks into 3D datasets for dimensional analysis. Techniques such as trilinear and cubic interpolation, as well as machine learning–based approaches, are commonly employed to improve reconstruction accuracy and visual quality. Comparative evaluation of these methods provides insight into their effects on alignment precision and computational

efficiency. Overall, effective image registration relies on the integrated application of these components and methodologies, and its continued development is supported by interdisciplinary research across fields such as medical imaging, remote sensing, and materials science, underscoring its broad relevance and importance in image analysis.

3.4.2. Image segmentation

Image segmentation is a critical step in visual data analysis, enabling the extraction of meaningful information from complex images and playing a key role in fields such as materials science, biology, and medicine. Despite advances in segmentation techniques, the process remains challenging due to limitations in image resolution and variability introduced by subjective human interpretation [48]. Different imaging modalities impose distinct resolution constraints and may generate artifacts or noise that complicate feature identification, while observer-dependent decisions can lead to inconsistencies and reduced reproducibility [49]. These challenges highlight the need for automated and objective segmentation approaches. Recent advances in machine learning, particularly convolutional neural networks (CNNs), have shown strong potential for improving segmentation accuracy and consistency compared to traditional threshold-based methods [50]. The accuracy of segmentation is also influenced by voxel transformation algorithms used to convert 2D image stacks into 3D datasets, as these transformations affect feature definition and continuity. In practice, segmentation involves separating objects of interest from the background, with thresholding being a simple and effective method when features exhibit distinct intensity contrasts, such as garnets in rock specimens. This approach converts grayscale images into binary images by assigning pixels to either object or background based on an intensity threshold (Fig. 6), though its success depends on image contrast, noise levels, and appropriate threshold selection.

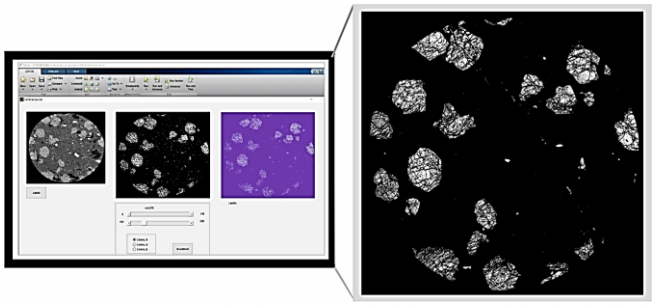

Figure 6. BSE image umbralization. On the left, image of the thresholded layer 50. On the right of the Toolbox visualization, realizing the umbralization.

3.4.3. Elimination of noise and parameterization of true color

Matlab, a high-level programming language with strong capabilities for matrix manipulation, was used to implement advanced algorithms for noise reduction in BSE images, a critical step for improving image quality prior to segmentation and 3D reconstruction [51]. Noise and artifacts can significantly affect image clarity and reconstruction accuracy, requiring robust filtering strategies. Regularization-based optimization approaches have been shown to effectively reduce noise and improve 3D reconstruction accuracy [52]. In this study, edge-preserving denoising algorithms were applied to BSE images to smooth intra-region variability while maintaining sharp mineral boundaries [53–54]. These filters enhance edge definition with minimal distortion, which is essential for accurate segmentation. Matlab also enabled precise parameterization of garnet color attributes, facilitating reliable identification and representation of mineralogical features. The resulting noise-reduced images improved segmentation performance and voxel transformation, leading to more accurate 3D reconstructions, as illustrated in Fig. 7. Overall, the application of Matlab-based noise reduction techniques significantly enhanced image quality and ensured reliable visualization and interpretation of rock microstructures.

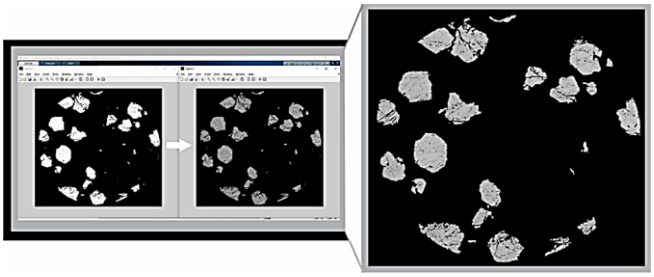

Figure 7. Visualization of Matlab Toolbox in the elimination of noise and parameterization of the true color, in the left layer 50 with the parameterization results and without noise.

After measuring the mineral particles, including the garnets visible in each layer, the next step involved assessing each individual grain. For this purpose, a specialized Matlab code named "measures" was developed, which facilitates the measurement of the maxi-mum and minimum dimensions of each garnet in micrometers. The results obtained from this analysis are automatically recorded in an Excel file, as illustrated in Fig. 8. Subsequently, the lengths of the maximum and minimum axes of 65 mineral particles were analyzed, as detailed in Table 1. It is important to highlight that certain particles were excluded from this analysis due to their positioning at the edges of the layer, which rendered their true sizes difficult to determine accurately. The estimated measurement error is re-ported to be within ± 0.01 µm, emphasizing the precision of the measurement process. To further contextualize these findings, it is essential to compare them with similar studies conducted by other researchers. This comparative analysis not only aids in validating our measurements but also contributes to a comprehensive understanding of the measurement process and its associated uncertainties. By examining the results alongside existing literature, we can better appreciate the variations and consistencies in mineral grain measurements, thereby enhancing the overall robustness of our findings.

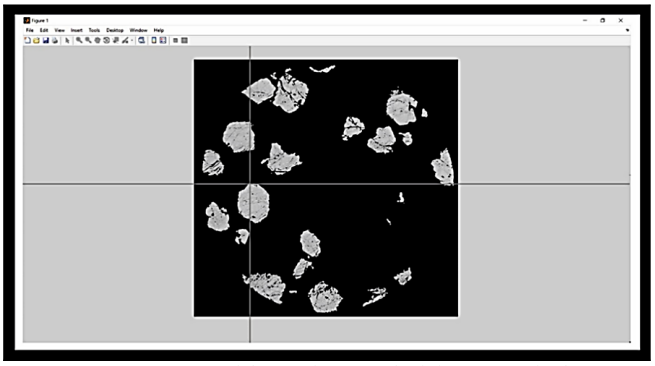

Figure 8. Measurement of the maximum and minimum axes in the garnet particles by means of Image Processing Toolbox.

Table 1. Measures of maximum and minimum axis in particles of garnet through the 50 sections layers (Garnet 1 to 18).

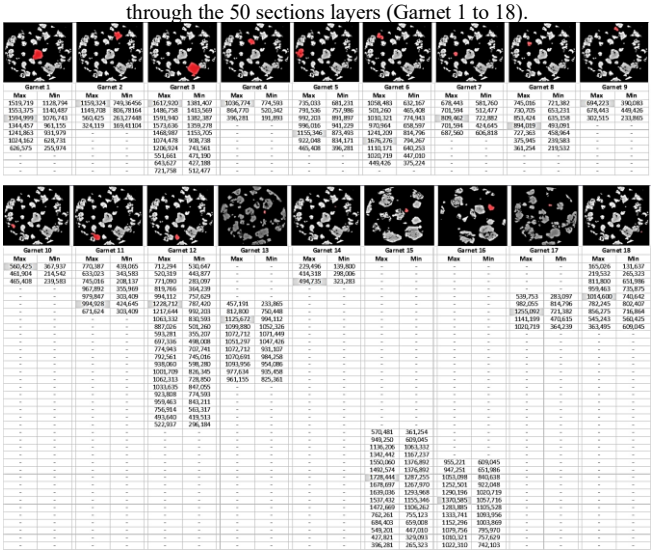

Garnet 1		Garnet 2		Garnet 3		Garnet 4		Garnet 5		Garnet 6		Garnet 7		Garnet 8		Garnet 9	
Max	Min	Max	Min	Max	Min	Max	Min	Max	Min	Max	Min	Max	Min	Max	Min	Max	Min
1519,719	1128,794	1559,324	749,36456	1612,920	1381,407	1036,774	774,583	735,033	681,231	1058,483	632,367	678,443	581,760	745,016	721,382	694,223	390,083
1553,375	1140,487	1149,708	806,78164	1486,758	1411,569	864,770	520,342	730,536	757,986	501,260	465,408	701,594	512,477	730,705	653,231	678,443	449,426
1594,999	1076,743	565,425	263,27448	1581,940	1381,397	896,181	191,893	992,203	891,897	1031,321	714,943	809,462	722,882	853,424	635,358	302,515	231,865
1344,457	961,155	324,119	169,41104	1573,636	1359,278	-	-	996,016	941,229	970,964	658,597	701,594	424,645	894,089	493,091	-	-
1241,863	931,979	-	-	1468,987	1353,705	-	-	1155,346	875,493	1241,209	854,796	687,560	606,818	727,363	458,964	-	-
1024,562	628,731	-	-	1074,478	908,738	-	-	922,048	834,171	1676,276	794,267	-	-	375,945	230,583	-	-
626,575	250,974	-	-	1206,024	743,561	-	-	465,408	396,283	1131,171	640,253	-	-	363,254	219,532	-	-
-	-	-	-	551,661	471,190	-	-	-	-	1020,719	447,030	-	-	-	-	-	-
-	-	-	-	643,627	427,198	-	-	-	-	446,426	375,224	-	-	-	-	-	-
-	-	-	-	721,758	512,477	-	-	-	-	-	-	-	-	-	-	-	-

Garnet 10		Garnet 11		Garnet 12		Garnet 13		Garnet 14		Garnet 15		Garnet 16		Garnet 17		Garnet 18	
Max	Min	Max	Min	Max	Min	Max	Min	Max	Min	Max	Min	Max	Min	Max	Min	Max	Min
560,425	367,937	770,387	438,065	712,294	530,647	-	-	229,496	139,800	-	-	-	-	-	-	365,026	131,637
461,904	214,542	633,023	343,583	520,319	443,977	-	-	414,318	298,036	-	-	-	-	-	-	219,532	265,323
465,408	239,583	745,016	208,137	771,080	281,097	-	-	694,735	323,283	-	-	-	-	-	-	811,800	651,986
-	-	967,892	355,969	819,766	364,239	-	-	-	-	-	-	-	-	-	-	959,463	735,875
-	-	979,847	303,409	994,112	757,629	-	-	-	-	-	-	-	-	539,753	283,097	1014,600	740,642
-	-	994,928	434,645	1228,712	787,420	457,191	233,865	-	-	-	-	-	-	982,055	814,796	782,245	802,407
-	-	671,624	303,409	1217,644	992,203	812,800	750,448	-	-	-	-	-	-	1255,092	721,382	856,275	716,864
-	-	-	-	1063,332	830,593	1125,672	994,112	-	-	-	-	-	-	1141,109	470,615	545,243	560,425
-	-	-	-	887,026	505,260	1099,880	1052,326	-	-	-	-	-	-	1020,719	364,239	363,495	609,045
-	-	-	-	591,381	355,207	1072,712	1021,449	-	-	-	-	-	-	-	-	-	-
-	-	-	-	697,106	498,008	1053,297	1047,416	-	-	-	-	-	-	-	-	-	-
-	-	-	-	774,943	701,741	1072,712	931,307	-	-	-	-	-	-	-	-	-	-
-	-	-	-	792,561	745,016	1070,691	984,258	-	-	-	-	-	-	-	-	-	-
-	-	-	-	938,060	598,280	1093,956	954,086	-	-	-	-	-	-	-	-	-	-
-	-	-	-	1001,709	826,345	977,634	935,458	-	-	-	-	-	-	-	-	-	-
-	-	-	-	1062,313	728,850	961,155	825,363	-	-	-	-	-	-	-	-	-	-
-	-	-	-	1033,635	847,055	-	-	-	-	-	-	-	-	-	-	-	-
-	-	-	-	923,808	774,591	-	-	-	-	-	-	-	-	-	-	-	-
-	-	-	-	959,463	845,211	-	-	-	-	-	-	-	-	-	-	-	-
-	-	-	-	756,914	563,317	-	-	-	-	-	-	-	-	-	-	-	-
-	-	-	-	493,660	439,513	-	-	-	-	-	-	-	-	-	-	-	-
-	-	-	-	522,937	296,184	-	-	-	-	-	-	-	-	-	-	-	-
-	-	-	-	-	-	-	-	-	-	570,481	361,254	-	-	-	-	-	-
-	-	-	-	-	-	-	-	-	-	940,250	609,045	-	-	-	-	-	-
-	-	-	-	-	-	-	-	-	-	1136,206	1063,332	-	-	-	-	-	-
-	-	-	-	-	-	-	-	-	-	1340,442	1167,237	-	-	-	-	-	-
-	-	-	-	-	-	-	-	-	-	1560,060	1376,892	955,221	609,045	-	-	-	-
-	-	-	-	-	-	-	-	-	-	1402,574	1376,892	947,254	851,986	-	-	-	-
-	-	-	-	-	-	-	-	-	-	1728,444	1287,255	1151,098	840,618	-	-	-	-
-	-	-	-	-	-	-	-	-	-	1639,697	1267,970	1252,501	922,048	-	-	-	-
-	-	-	-	-	-	-	-	-	-	1639,036	1293,968	1290,196	1020,719	-	-	-	-
-	-	-	-	-	-	-	-	-	-	1507,432	1355,346	1330,985	1057,716	-	-	-	-
-	-	-	-	-	-	-	-	-	-	1472,669	1306,262	1281,885	1305,528	-	-	-	-
-	-	-	-	-	-	-	-	-	-	762,261	755,123	1333,741	1093,956	-	-	-	-
-	-	-	-	-	-	-	-	-	-	684,403	659,008	1152,296	1003,869	-	-	-	-
-	-	-	-	-	-	-	-	-	-	549,201	447,013	1079,716	795,970	-	-	-	-
-	-	-	-	-	-	-	-	-	-	427,921	329,093	1083,521	757,629	-	-	-	-
-	-	-	-	-	-	-	-	-	-	396,281	265,323	1022,310	742,103	-	-	-	-

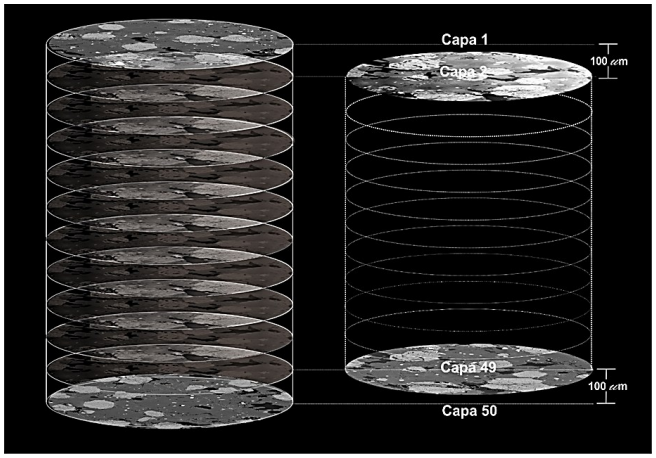

Figure 9. Stack of the high-resolution mosaics of BSE images corresponding to the analyzed layers of the garnet-bearing metamorphic rock.

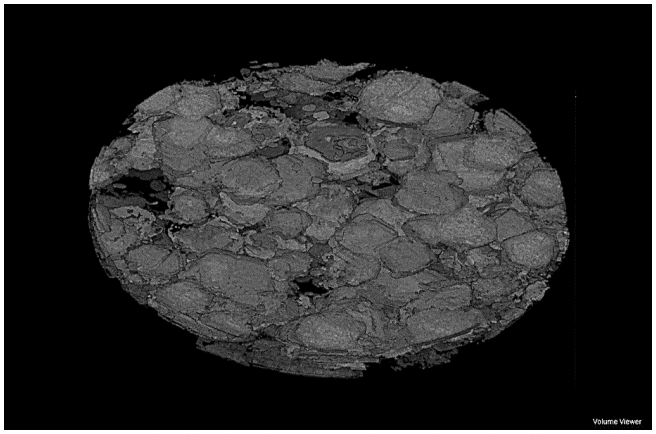

Figure 10. 3D visualization of corresponding to the analyzed layers of the garnet-bearing metamorphic rock.

3.5. 3D visualization

Serial sectioning was performed by cutting 50 parallel layers, with an initial spacing of 500 µm between layers 1 and 10. To improve garnet particle retention, the spacing was reduced to 250 µm between layers 11 and 50 (Fig. 9), minimizing the loss of structural information during sectioning. To support 3D reconstruction of the garnet PSD while optimizing memory usage, the open-source software ImageJ was employed. ImageJ, a public-domain image processing program developed at the U.S. National Institutes of Health, has been widely used in similar 3D mineral reconstruction studies [50], although variations in sectioning parameters may influence particle preservation. Figure 10 shows the miniplug rock volume and the resulting 3D spatial distribution of garnet, representing particle measurements across the entire sample. The reconstructed volume corresponds to the 50 serial sections, with a total cut depth of 5.5 mm. This approach enabled a comprehensive visualization of garnet spatial distribution within the sample, providing insight into its internal arrangement and textural characteristics.

3.6. Particle size distributions (PSDs)

Petrographic information has significant quantitative links with the crystallization kinetics, with PSDs serving as essential complements to laboratory kinetic studies. Previous research on metamorphic rocks, such as that by Marsh [13], Cashman and Ferry [14], and Waters and Lovegrove [55], highlights the critical role of PSDs interpretation in understanding the nucleation and growth conditions of mineral phases. Such interpretations provide valuable insights into various factors, including nucleation and growth rates, growth durations, and heat fluxes during metamorphism. In this study, we explore the PSD of garnet within a metamorphic rock of the Arquía Complex, aiming to enhance our understanding of its dynamic history. To calculate the PSD, we measured both the major and minor axes of 65 garnet particles across 50 sectioned layers, using BSE image mosaics. According to Higgins [56-57], the intersection length statistically corresponds to the actual particle length, while the intersection width approximates its

intermediate dimension. In this context, the major axis of the particle is considered the actual particle size, determined by the maximum value observed in each layer. The measured axis values range from 494 to 2752 µm, so we selected a size range of 300 µm, generating five size classes. To model the PSD of garnets from the Arquía Complex, exponential, Gaussian, and hyperbolic tangent functions were evaluated. The observed PSD exhibits a clear asymmetry, with early-nucleated garnets reaching larger sizes and later-nucleated ones remaining smaller. This pattern is not adequately captured by Gaussian distributions, which assume symmetry, nor by exponential functions, which predict a monotonic decay without reflecting the accumulation of intermediate-sized garnets. In contrast, the hyperbolic tangent function: $n(L) = n_o \tanh(L\text{-}L_o/b)$, provides a better fit to the observed PSD, reflecting both the initial high nucleation rate and the growth competition among crystals. The hyperbolic tangent shape allows modeling how early-nucleated garnets grow faster and attain larger sizes, while later-nucleated garnets are limited by available space and resources, producing a tail of smaller particles. Physically, this behavior is associated with spatial and temporal variations in nucleation and growth during regional metamorphism, where temperature and pressure conditions evolve progressively, leading to a non-uniform crystallization history. Therefore, the choice of the hyperbolic tangent model is justified not only statistically but also physically, as it integrates the kinetic history of garnet nucleation and growth observed in the Arquía Complex. To ensure accurate size determination, we compared the stereological method applied to thin sections and digital photographs of 2D data with the actual values obtained through serial sectioning. This meticulous approach strengthens the reliability and validity of our results, improving the quality of our analysis and contributing to a deeper under-standing of garnet's dynamic history within the metamorphic rocks of the Arquía Complex. To generate the size frequency histogram, we calculated n, which is determined by dividing the number of data points in each specified range by the set interval. This leads to *NV*, calculated by dividing n by the rock sample volume, thus creating the *y*-axis of the histogram. The selected ranges are plotted on the *x*-axis. The volume of the plug is calculated using the Eq. (1):

$$V = \pi r^2 h \tag{1}$$

Where, π is a known value, r is the radius of the rock plug and h is derived from the working distances found under SEM conditions and the BSE images. Quantifying texture can be achieved by measuring the number of particles per unit rock volume within a specific size range (ΔL). This quantification is expressed as the population density $n(L)$, where L denotes particle size. Achieving equilibrium requires knowing the particle density as a function of size. However, due to challenges in making precise size measurements within small ΔL ranges, it is more practical and insightful to work with a cumulative distribution derived from the histogram function $n(L)$. This cumulative distribution provides a comprehensive view of the PSD within the rock sample, facilitating a deeper understanding of its textural characteristics.

To analyze grain growth rates, we have also included a temporal component in the PSD interpretation. Eq. (2) represents the numerical density, which can be useful for understanding the PSD of garnets in different types of metamorphic rocks, providing information on metamorphic conditions.

$$n(L) = \frac{dN(L)}{dL} \tag{2}$$

Where, $N(L)$ is a function describing the total number of particles with size equal to or smaller than L (i.e., numbers of particles per unit volume). $N(L)$ is also a simpler and more reliable measure, in which a progressive sum is formed, providing a very stable series, from which information about any choice of ΔL can be derived.

From Eq. (1), the population density of particles can be obtained through Eq. (3), which describes the population density $n(L)$ derived from an infinite number of intervals such that ΔL approaches zero.

$$n(L) = \frac{dN(L)}{dL} \tag{3}$$

Where, n(L) is the fundamental variable of PSDs and n is the number of particles in a given size class and per unit volume. The garnet particles within the metamorphic rock under analysis show a wide range of sizes, effectively illustrated through histograms (Fig. 11). As noted by Waters and Lovegrove [55], practical measurements of particle diameters involve sections through the rock, requiring consideration that not all particles are cut through their center. Histograms often show a bell-shaped pattern, commonly known as a "normal distribution", where points are equally likely to occur on both sides of the mean. A relevant observation is that these histograms can be interpreted, from right to left, as a representation of the nucleation rate over time. Particles of garnet that nucleated in early stages tend to have grown to larger sizes, while later stages show a decreasing nucleation rate, resulting in smaller particle sizes, which suggests that particle growth in the metamorphic system was influenced by fluctuations in nucleation rates. This behavior of the PSD resembles more of a hyperbolic tangent function (*tanh*), rather than an exponential function. This shape can be interpreted as a transition in the growth regime, reflecting how environmental factors such as temperature and pressure influence crystal development over time. Although this study has applied a fitting model based on a hyperbolic tangent function to represent the PSD of garnet in the metamorphic rocks of the Arquía Complex, it is important to acknowledge that Gaussian distributions, while useful, may not always fully capture the complexities of mineral nucleation and growth processes. Phenomena such as Ostwald ripening or heterogeneous nucleation conditions could lead to significant deviations from a standard Gaussian fit, especially in samples

affected by temperature or composition gradients. However, this study should be considered preliminary, and many of these aspects are be-yond the scope of this work due to limitations in data resolution and the natural variability of metamorphic systems. Future research could focus on incorporating these factors to achieve a more detailed and accurate interpretation of the dynamic history of garnet nucleation and growth in metamorphic environments.

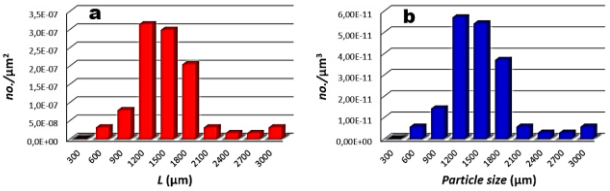

Figure 11. Frequency histograms with respect to (a) particles per area unit (NA) and (b) particles per volume unit (NV).

The shape of the PSD is primarily controlled by temporal changes in nucleation rate, as highlighted by Waters and Lovegrove [55]. The right-hand tail of the distribution, often resembling an exponential function, reflects the initial acceleration of nucleation and the rapid formation of smaller garnet crystals. Grain growth rates can be quantified by comparing observed garnet growth with theoretical nucleation and growth models. Figure 12a shows the cumulative frequency, featuring an inflection point that may indicate a transition in growth regime influenced by environmental factors such as temperature and pressure. Alternatively, plotting the natural logarithm of population density (n) against particle size (L) linearizes the PSD, facilitating comparison and analysis, as applied in fields such as chemical engineering [16] and igneous petrology [5,13–14]. This approach aids in interpreting the statistical distribution of particle sizes and the dynamics of crystal growth. If we interpret the results from Fig. 12a as a hyperbolic tangent, its derivative is $cosh^{-2}$, which visually fits the experimental data much better. Figure 12b shows the relationship between $ln(n)$ and L, which may not be entirely linear due to the nature of the experimental data. These data fit better to a model based on the hyperbolic tangent. Although this relationship is still useful, it should not be extrapolated linearly as if it were an exponential function. The interpretation of garnet nucleation and growth in this context should be revisited based on the hyperbolic tangent model, as it better reflects the experimental data obtained.

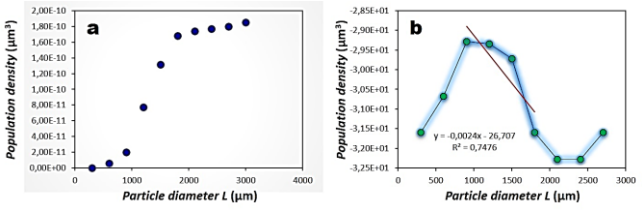

Figure 12. (a) Cumulative frequency. (b) ln(n) vs. L diagram.

The revised model now incorporates a comparison with growth rates derived from theoretical nucleation models, enhancing the analysis of crystallization dynamics. We also fit the experimental data to the hyperbolic tangent function to better represent the observed nucleation and growth patterns. However, the observed behavior on the right-hand side of the PSD of the analyzed garnet-bearing amphibolite presents an approximate linear trend, which has been characterized by an exponential equation, as proposed by Cashman and Ferry [14] and Waters and Lovegrove [55]. This exponential model, commonly ex-pressed as Eq. (4), effectively describes the relationship between particle size and population density, providing key insights into the nucleation and growth processes affecting garnet formation within the rock sample.

(4) $n = n_0 e^{-bL}$

Where n is the population density, n^o is the intercept at $L = 0$, b is a constant that de-scribes the slope of the linear graph, and L is the particle size. However, instead of using an exponential model as in Eq. (4), the data obtained suggest that the PSD follows a behavior that fits better with a hyperbolic tangent, in the form $N(L) \sim tanh[(L\text{-}L_o)/b]$. This function has a derivative that approximates $cosh^{-2}[(L\text{-}L_o)/b]$, providing a better visual and mathematical description of the observed experimental data. This improved adjustment in the interpretation of the PSD provides a more accurate and robust insight into the dynamic his-tory of nucleation and growth of garnet in the metamorphic rocks of the Arquía Complex. The exponential relationship, expressed Eq. (4), commonly used in similar studies, is no longer directly applicable in this case. Instead, the hyperbolic form (Eq. (5)) provides a more accurate description of the observed distribution:

$$n = n^o tanh\left[\frac{(L\text{-}L_o)}{b}\right] \quad (5)$$

Where no is the initial particle density and b is a parameter that describes the slope of the graph. This formula provides a better fit to the behavior observed in the experimental data.

The calculations derived from this model not only provide a better representation of garnet nucleation and growth, but also offer a tool for reconstructing the thermal and dynamic history of the studied rocks.

The total number of particles (N_T) in the garnet-bearing metamorphic rock can be determined by Eq. (6).

$$m_0 = N_T = \int_0^\infty n_0 e^{-bL} dL = \frac{n_0}{b} \quad (6)$$

Where, L is equivalent to the zero moment of the distribution. Eq. (7) represents the total length of the particles.

$$m_1 = L_T = \int_0^\infty L n_0 e^{bL} dL = \frac{n_0}{b^2} \quad (7)$$

The average size of the particles ($\bar{L}$) can be determined from Eqs. (6) and (7) by Eq. (8), which represents the average length of particles.

$$\bar{L} = \frac{L_T}{N_T} = \frac{1}{b} \quad (8)$$

From Fig. 12b, the values of b and no calculated as -0.0024 μm^{-1} and -26.707μm^{-1}, respectively, which can be replaced in

the exponential equation as n = -26.7070$e^{0.0024L}$ to solve Eqs. (6), (7) and (8). The values obtained for N_T, L_T and $\bar{L}$ were 10994.81 µm (1.10 cm), 4526325.34 µm (452.63 cm) and 411.68 µm (0.04 cm), respectively.

These equations provide a quantitative view of the PSD of garnets in metamorphic rocks. The information derived from these calculations is invaluable for reconstructing the geological history of the area, understanding the metamorphic processes that occurred, and evaluating the quality and potential of the mineral resources present in the rock. Additionally, they contribute to the modeling of geological processes and may have implications in fields such as petrology and economic geology.

3.7. Nucleation and growth rates and growth times

The PSD reveals not only the range of particle sizes within a rock sample but also provides insights into crystallization timescales, which are controlled by growth (G) and nucleation (J) rates. By analyzing the PSD, researchers can infer the duration of crystallization and the thermal and chemical conditions during rock formation. The slope of the cumulative distribution, expressed as population density (n, number per volume per size range), serves as a key indicator of particle distribution [58]. Typically, distributions show a linear segment followed by a bell-shaped curve near the y-axis, with the slope and vertical intercept reflecting the dynamics of nucleation and growth. Steeper slopes suggest rapid nucleation relative to growth, whereas gentler slopes indicate prolonged growth or lower nucleation rates. These parameters are essential for interpreting the crystallization history and reconstructing the environmental conditions that influenced mineral formation, offering a deeper understanding of the rock's petrogenetic evolution.

According to Blundy and Cashman [58] a PSD relates the average rates of nucleation (J) and growth (G). It is assumed that the dominant size (dL) is a consequence of the stable particle growth at an appropriate time (t), then $dL = G_\tau$, where t is the effective crystallization time. The nucleation rate is given by $J = dNv/dt$, where Nv is the number of particles per unit volume. In turn, the nucleation rate is related to the growth rate $J = n°G$, where $n°$ is the number of nucleated particle density (intercept with zero), so that the time can be determined for any distribution if knows G. We can also define an average growth time (t) as a function of L, and a linear average growth rate G.

The average growth time and nucleation rate are given by Eqs. (9) and (10), respectively.

$$\bar{t} = \frac{\bar{L}}{\bar{G}} \tag{9}$$

$$J = \frac{N_T}{\bar{t}} \tag{10}$$

Therefore, a linear particle size plot encapsulates measurable parameters that can be directly correlated with particle nucleation rates, growth rates, and growth times. As depicted in Eq. (9), there exists a dependence between the parameters of t (growth time) and G (growth rate). Consequently, it becomes imperative to ascertain certain parameters to de-rive the average nucleation rate. Cashman and Ferry [14] introduce Eq. (11), which delineates the growth rate based on variations in mass over time. This equation serves as a fundamental tool in quantifying the growth dynamics of particles within the system under examination.

$$\frac{dm}{dt} = \frac{K\Delta S(T - T_{eq})}{RT} \tag{11}$$

Where dm/dt is the mass transfer rate in moles per square centimeter of surface per second, K is a rate constant, ΔS is the enthalpy of the reaction, (T-T_{eq}) = ΔT corresponds to the excess of the reaction, R is the gas content in $K^{-1}mol^{-1}$ and T is the temperature of the reaction. According to Walther and Wood (1984), the rate constant K is influenced by temperature and composition across various mineral species. Their findings suggest that, within experimental uncertainty (approximately half the order of magnitude), a wide array of minerals exhibit similar rates at any given temperature. Consequently, at elevated temperatures, heterogeneous reactions persist with rate constants approximately governed by Eq. (12), also known as the velocity constant. This observation underscores the importance of temperature and composition in dictating reaction kinetics and highlights the generalizability of rate constants across diverse mineral species under certain conditions.

$$logK = \frac{-2900}{T} - 6.85 \tag{12}$$

Where T is in °K and the rate constant has been converted from mole $cm^{-2}s^{-1}$ to atom grams of oxygen $cm^{-2}s$. Eq. (12) appears to be maintained for the most relevant metamorphic fluid compositions and for all minerals for which data are available. Finding the velocity constant and dm/dt only equalizes Eq. (11) with respect to the length. Eq. (13) represents the linear growth rate.

$$\frac{dr}{dt} = \frac{dm/dt}{W} \tag{13}$$

Where r is the radius of the particle and W is the normalization of the equation, i.e., the atom-grams of oxygen per cm^3. In this way, when the value of dr/dt is known, the aver-age growth rate G is being obtained and the growth times and the average nucleation rates can be obtained.

Standardization is carried out by Eq. (14), which represents the number of atom grams of oxygen and also represents the volume of a sphere, which associates with a spherical behavior of the mineral and w the atom-grams of oxygen present in the chemical formula of garnet.

$$w = \frac{4}{3}r^3W \tag{14}$$

Considering Eqs. (11), (12), (13) and (14), it is possible to determine the average nucleation rate, the time of growth and the average growth rate. In order to find the velocity constant, the temperature value of 600 °C is taken, according to the

metamorphic facies of Barker [59], it is necessary that the temperature value is expressed in °K. Replacing in equation 11, a value of $K = 6.73x10^{-11}$ atom gram of oxygen/cm^{2}s^{-1} is obtained. To determine the values of the mass transfer rate dm/dt, it is necessary to take into account that $K = 6.73x10^{-11}$ gram atom of oxygen per cm -2 s^{-1}. ΔS = unknown value. Therefore, Walther and Wood (1984) propose: ΔS = 1 cal/mol^{-1} °C for a lower limit and ΔS = 20 cal/mol^{-1} °C for an upper limit; (T-T_{eq}) = ΔT = 1 °C; R = 1.9872 cal. Mol. K; T = 873 °K. ΔT was taken as 1 °C, the lower limits for ΔT were obtained from warming rates of 1°/104-1°/106 years (warming rates suggested by Walther and Wood [60]).

Replacing in Eq. (11): dm/dt = $7.76x10^{-13}$ oxygen gram atom/cm^{2}s

From Eq. (14) W is cleared, which is the normalization of the garnet equation to units of grams of oxygen/cm3, so that the Eq. (15) would be:

$$W = \frac{3w}{(4\pi r^3)} \tag{15}$$

Where W are the atom-grams of oxygen present in the particle of garnet on the inverse of the volume of the particle. To obtain this value it is necessary to know the crystallography of the garnet. The chemical composition of garnets is variable. We substitute x in the equation for the value of the temperature and obtain the value of a in Angstroms. For a temperature of 873 °K, a = 11.58 Å. With the parameter a = r it is possible to calculate the volume of the almandine garnet particle, starting from the concept of the Eq. (16) where a spherical volume is assumed for the garnet, according to Walther and Wood [60].

$$V = \frac{4}{3}\pi r^3 \tag{16}$$

$V = 6.5x10^{-21}$

Taking a second approximation according to the crystallization of the garnet as a do-decahedron cubic system, the dodecahedron volume is expressed by Eq. (17) as:

$$V = 16\frac{\sqrt{3}}{9}a^3 \tag{17}$$

$V = 4.8x10^{-21}$

The volume values of the mineral fall within an acceptable range for the objectives of this study. To proceed with the calculation of the volume of the dodecahedron, considering the crystalline structure of the mineral, it is necessary to determine the number of gram atoms present in the mineral. In order to replace in Eq. (15) for normalization, we must first determine the number of gram atoms present in the mineral. This can be calculated by di-viding the atomic weight of oxygen by Avogadro's number. Then, we can substitute this value into Eq. (18).

$$W = \frac{2.66x10^{-23}}{4.77x10^{-21}} = 0.006 \tag{18}$$

With the value obtained from normalization is replaced in Eq. (19).

$$\frac{dr}{dt} = \frac{7.76x10^{-13}\ \text{atom-gram of oxygen/cm}^2\text{s}}{0.006\ \text{atom-gram of oxygen/cm}^3} = 1.4x10^{-10}\ \text{cm/s} \tag{19}$$

,

which corresponds to the linear average growth rate G. With the values of G and $\bar{L}$ (average size of the particles), we obtain the growth time contemplated in Eq. (9) and then the average nucleation rate given in Eq. (10), with N_T as depicted in Table 2. Then, the average values obtained for J, G and t can be calculated. By integrating these equations, researchers can derive average nucleation rates, growth times, and growth rates, which are fundamental for reconstructing the crystallization history of garnet in metamorphic rocks. Understanding these parameters allows geo-scientists to make inferences about the conditions of metamorphism, such as pressure, temperature, and the fluid composition of the environment during rock formation. This comprehensive approach not only elucidates the processes that led to garnet formation but also aids in predicting how similar minerals may behave under varying geological conditions, thereby enhancing our overall understanding of metamorphic petrology.

Table 2. Data of nucleation and growth rates and growth times.

Teq	$\bar{L} = 1/b$	$G = dr/dt$		N_T	t		n_o	J
°C	cm	cm/s		cm	years		cm^{-4}	cm^{-3}/s
		ΔS = 1 cal/°C	ΔS = 20 cal/°C		ΔS = 1 cal/°C	ΔS = 20 cal/°C	ΔS = 20 cal/°C	ΔS = 20 cal/°C
600	$4.12x10^{-2}$	$6.99x10^{-12}$	$1.4x10^{-10}$	1.1	186.74	9.34	$2.67x10^{-3}$	$3.73x10^{-9}$

3.8 Metamorphic implications and P–T context

The particle size distribution and growth history of garnets in the Arquía Complex provide direct insights into the metamorphic evolution of the region. The coexistence of early-formed large garnets and later-formed smaller ones indicates prolonged nucleation under progressively changing conditions, consistent with regional amphibolite-facies metamorphism of basaltic protoliths. The larger garnets likely crystallized during peak metamorphic conditions, reflecting high temperatures and pressures, whereas smaller garnets formed during cooling or decompression stages, highlighting a dynamic P–T path. Moreover, the variation in garnet size and growth rates reflects heterogeneous nucleation kinetics, implying that metamorphic reactions were influenced by localized differences in chemical potential, fluid availability, and strain distribution. This supports a model of progressive metamorphism within a geodynamically active orogenic belt, where tectonic processes such as crustal thickening, exhumation, and shear zone activity modulated garnet crystallization. From a geodynamic perspective, the PSD analysis suggests that garnet growth is sensitive to the thermal gradient and deformation history, providing a link between microstructural textures and regional tectonics. Thus, the detailed 3D reconstruction and PSD modeling not only quantify crystallization kinetics but also serve as petrological proxies for reconstructing P–T-t paths and understanding metamorphic processes within the Colombian Andes. In this way, garnet textures become powerful indicators of orogenic evolution, thermal regimes, and the interplay between metamorphism and deformation in the Arquía Complex.

3.9. Experimental uncertainties and error analysis

The precision and reliability of our garnet PSD and growth measurements are inherently linked to experimental limitations, which must be carefully considered to contextualize the results. Key sources of uncertainty include: Spatial resolution of serial sections: Sections were cut at 100 µm thickness, with initial layer spacing of 500 µm reduced to 250 µm for layers 11–50. While this spacing ensures retention of garnet particles, the z-axis resolution is coarser than the xy-plane resolution (~1.65 mm × 1.24 mm mosaics), potentially averaging fine microstructural details. Thinner sections would improve resolution but increase noise, acquisition time, and computational demand.

Image acquisition and stitching: BSE imaging produces high-resolution mosaics; however, minor misalignments during stitching or slight distortions from mechanical polishing may introduce systematic errors in particle boundary definition. Edge effects, particularly for garnets at section borders, contribute to underestimation or overestimation of true particle dimensions.

Segmentation and noise reduction: Threshold-based segmentation and edge-preserving denoising algorithms in MATLAB provide reproducible identification of garnet boundaries. Nevertheless, variations in image contrast, residual noise, or overlapping grains can cause minor inaccuracies in size measurements.

Measurement reproducibility: Maximum and minimum axes were measured for 65 garnets, with an estimated error of ±0.01 µm. Although highly precise, this error does not account for potential biases from particle orientation relative to the cutting plane or partial particle truncation.

Volume estimation and shape assumptions: Particle volumes were approximated as spheres or cubic dodecahedra. Real garnet shapes deviate from these idealized geometries, introducing additional uncertainty in mass transfer and growth rate calculations.

In general, while these uncertainties may slightly affect absolute PSD values and growth rates, the systematic approach, precise sectioning, controlled polishing, automated image processing, and 3D reconstruction, minimizes random errors and ensures that observed trends in nucleation timing, size distribution, and metamorphic implications are robust and reproducible.

4. Discussion

The methodology employed in this study for rock sample preparation, serial sectioning, image acquisition, and 3D reconstruction has proven to be highly effective, achieving significant advancements compared to previous techniques. Below, various key aspects of this research are detailed, organized into subsections.

4.1. Advances in sample preparation and sectioning

Compared to previous methods documented by Terrell and Higgs [18] and Liao *et al*. [19], where significant polishing errors were observed, our approach distinguishes itself through a more precise control of parameters such as speed and load during the polishing process, resulting in more accurate and uniform sections. When choosing between mechanical polishing and other polishing methods, such as ionic polishing, the decision largely depends on the material being processed and the level of precision required. Mechanical polishing is a widely used and cost-effective method for many applications, it may not provide the ultra-smooth, uniform surface needed for high-precision analysis, especially in scientific research [61-62], whereas ionic polishing offers a much more controlled and fine finish, making it ideal for preparing samples for electron microscopy and other high-resolution techniques [63-65]. Table 3 shows is a detailed comparison of the key differences between these two polishing methods, highlighting their respective ad-vantages and limitations.

Table 3. Differences between mechanical polishing and ionic polishing.

Characteristic	Mechanical Polishing	Ion Polishing
Process	Uses physical abrasives to remove layers from the rock surface.	Bombards the surface with accelerated ions (such as argon, gallium, or boron) to polish in a controlled manner.
Required equipment	Polishing machines with abrasive discs, water, and oils.	Ion polishing systems like focused ion beam scanning electron microscope (FIB-SEM), gatan precision ion polishing system (Gatan PIPS), and other ion-based sample preparation systems.
Type of finish	A polished surface, though there is a risk of scratches or marks if abrasives are not properly controlled.	An exceptionally smooth, fine, and uniform surface finish, ideal for microscopic observation.
Common applications	Preparation of thin sections of rocks, decorative stones, jewelry, and industrial materials.	Sample preparation for electron microscopy, high-precision materials, and the handling of delicate surfaces.
Process control	Manual control of pressure and abrasive materials.	Precise control of ion energy, ion type, time, and bombardment angle.
Durability of finish	Less durable if not maintained properly, with a risk of marks.	More durable finish, as the process doesn't damage the surface structure.
Environmental impact	Generates abrasive residues and dust.	Produces fewer physical residues, but energy is used to generate the ion beam, and microscopic debris may be produced.

This study addresses the challenges of rock sample preparation by optimizing mechanical polishing. Mechanical polishing is cost-effective, versatile, and efficient, making it suitable for a wide range of rocks and for processing larger sample volumes. However, it can cause surface scratches, generate abrasive residues, and produce less uniform finishes if not carefully controlled. To minimize these drawbacks, principles of optimized material removal, such as those proposed by Khan *et al*. [20] for optical components, can be adapted to improve precision in geological samples. Ion polishing (e.g., FIB-SEM) produces ultra-smooth, highly precise surfaces with minimal damage, making it ideal for high-resolution SEM or TEM analyses. It allows precise control over ion energy, type, and bombardment angle, but it is expensive, slower, limited to small areas, and requires specialized facilities and vacuum conditions. While FIB-SEM can yield higher resolution in 3D reconstructions, it is impractical for millimeter-scale rock volumes due to cost, processing time, and sample size limitations. For this study, mechanical polishing was selected to prepare a rock miniplug for 3D reconstruction. This approach enabled progressive abrasion of flat surfaces, efficient SEM analysis, and optimized workflow for multiple surface preparations. Mechanical polishing is faster, flexible, and accessible,

particularly for heterogeneous or larger rock samples, and it provides sufficient resolution for 2D visualizations and structural analysis at the desired scale. This methodology aligns with recommendations by Jerram and Higgins [3] regarding sample thickness and cutting planes, ensuring high-quality 3D reconstructions while balancing precision, efficiency, and accessibility. For reconstructing a full rock volume in 3D, mechanical polishing is a more effective option, especially for millimeter-sized samples. This technique allows for faster material removal and requires less preparation time compared to ion polishing used in the FIB-SEM, which is more suited to small volumes and requires more processing time. Moreover, mechanical polishing is a flexible and versatile technique that adapts better to different types of rocks, especially those with heterogeneous structures and varied hardness. In comparison, the FIB-SEM has limitations regarding the sample size it can process and requires strict preparation protocols. Mechanical polishing is also much faster than ion polishing methods like those used in the FIB-SEM, which involve longer preparation times and are less efficient for larger volumes. Since 3D reconstruction of a rock sample involves preparing multiple surfaces, mechanical polishing allows for a more streamlined process, accelerating the workflow and enabling quicker preliminary results. This enhanced workflow aligns with the methodologies recommended in previous studies, such as those by Jerram and Higgins [3], ensuring that sample preparation optimizes data interpretation and quality analysis. Although the FIB-SEM offers higher resolution, we determined that the level of detail required for our research did not necessitate the extreme precision offered by this technology. In this context, mechanical polishing provided a sufficient finish for obtaining 2D visualizations of polished surfaces and structural features at the desired scale, without the excessive resolution offered by the FIB-SEM. Furthermore, mechanical polishing is more accessible, as it can be performed in a variety of laboratories with less complex equipment, whereas the FIB-SEM requires specialized facilities. Furthermore, our approach adheres to previous recommendations regarding the management of sample thickness and cutting planes, which directly support the quality of the 3D reconstruction. This approach aligns with Khan *et al*. [20], who emphasize using mathematical models to optimize material removal and enhance sample quality. The selection of a 100 µm section thickness balances efficiency and uniformity in 3D reconstruction while facilitating clearer visualization of microstructural features, as recommended by Jerram and Higgins [3]. Adopting a methodology that minimizes ambiguities in cutting surfaces supports their guidance on selecting appropriate cutting planes for reliable analysis. The use of abrasive papers with grit sizes of 220 and 400 can cause crystal loss from the surface, potentially compromising the mineral record across layers [5,66]. In this study, this phenomenon was observed, and we recommend preparing additional polished surfaces to reduce crystal loss and improve 3D visualization. A notable limitation of the current reconstruction method is the low resolution along the z-axis during serial sectioning of garnet shapes [67], which can obscure details of their 3D morphology. To address this, fine-tuning acquisition parameters such as voxel size and scanning area is advised to enhance resolution, data interpretation, and the precision of 3D visualizations, consistent with prior recommendations for optimizing similar analyses [3].

4.2. Image acquisition and processing

The acquisition of BSE images has generated a robust dataset that enables detailed analysis of the microstructure of garnets. The use of Microsoft Image Composite Editor for image stitching has been supported by previous research [25-26], highlighting its effectiveness in creating image mosaics from microscopic datasets. The production of a high-resolution mosaic provides rich visualization that facilitates the precise identification of textural features in the analyzed samples. This approach differs from previous methods by providing higher resolution and more precise visualization of textural features, which improves the quality of analysis compared to traditional techniques. Image segmentation, performed using thresholding techniques, aligns with methodologies discussed by Khan and Ravi [48], who emphasize the relevance of this process for extracting meaningful information from images. Through noise reduction and color parameterization, we have achieved a refined approach that enhances the identification and analysis of garnets in the studied sections. Regarding image segmentation, we utilized a thresholding technique, which has been widely supported by the literature [48], which emphasizes the importance of this process for extracting meaningful information from microscopic images. To address concerns about the insufficiency of the analysis, we have refined the noise reduction and color parameterization processes, making the approach more robust and precise. This refinement is a significant improvement over previous studies that did not implement these techniques in as much detail.

4.3. 3D Visualization and particle size distributions

The 3D reconstruction of the PSD of garnet not only complements previous studies by Marsh [13] and Cashman and Ferry [14], but also provides a more precise quantitative framework for assessing nucleation and growth conditions within the Arquía Complex. The observed relationship between PSD and nucleation time supports earlier findings, indicating that larger garnets are associated with early nucleation events. Our analysis of the PSD reveals a bell-shaped curve in the fine to medium crystal size range, followed by a straight line with a negative slope, indicating a decrease in population density with increasing grain size. At the same time, our results suggest that phenomena such as Ostwald ripening [14] may influence the shape of the distribution, particularly in the growth stages of larger garnets. This interpretation expands upon the traditional view by proposing that Ostwald ripening could be influencing the

distribution of larger crystals, which was not previously considered in earlier studies. This interpretation diverges from reports by Kretz [68] and Galwey and Jones [69], who attributed the shape of crystal size histograms to variations in nucleation rates over time. The results of our PSD analysis align with the exponential model discussed in the literature, validating our approach to characterizing the dynamics of nucleation and growth. This analysis al-so emphasizes the importance of nucleation and growth rates in the evolution of metamorphic rocks, providing a deeper understanding of their geological history and dynamics.

4.4. Implications for future research

The implications of this study are significant for future research in petrology and geology. The refined methodology improves both the accuracy and resolution of data, establishing a precedent for using advanced imaging and analysis techniques in similar investigations. Future studies should apply this approach to other geological contexts, potentially revealing new insights into mineral formation and rock evolution. Specifically, correcting existing models to better represent dm/dt [60], examining the influence of rock texture and composition on PSD, and exploring alternative PSD measurement techniques could enhance understanding of crystallization dynamics. The role of Ostwald ripening [70,71], particularly during the early stages of garnet growth when small nuclei are unstable, warrants further investigation. A limitation of the current method is the low z-axis resolution during serial sectioning, which reduces fidelity in 3D garnet shapes. Future research could address this using high-resolution X-ray tomography, optimizing voxel size to improve 3D reconstructions and more precisely capture garnet nucleation and growth. Complementary techniques, such as infrared digital holography [15], could provide real-time observations of crystallization, phase behavior, and microstructural evolution, offering additional insights beyond BSE-based analysis. By integrating these approaches, researchers could better understand the influence of rock texture, composition, and metamorphic conditions on garnet PSD and growth dynamics. Overall, this study advances the understanding of garnet microstructure in metamorphic rocks and establishes a methodological framework for future research. Validation against previous studies demonstrates the robustness of our approach and highlights opportunities to explore nucleation and growth mechanisms in greater detail.

5. Conclusions

This study presents a novel methodology for studying garnet nucleation and growth in metamorphic rocks, combining precise serial sectioning and advanced imaging techniques. The key contribution of this work lies in the development of a robust, reproducible process for three-dimensional (3D) visualization of garnet morphology and the quantification of nucleation and growth rates. Through systematic adjustments to section thickness and grinding parameters, we have minimized errors and generated a high-quality dataset that provides an unprecedented level of detail regarding garnet morphology. This methodology not only addresses existing challenges in imaging and analyzing metamorphic minerals but also sets a standard for similar studies in the future.

The analysis of PSDs reveals a clear relationship between nucleation timing and particle size, providing valuable insights into the crystallization conditions within the Arquía Complex. Our findings confirm that earlier nucleation events lead to the formation of larger garnets, while later events are associated with smaller particles. This relationship offers new understanding into the crystallization dynamics and provides a clearer picture of the evolutionary history of garnet in metamorphic environments.

However, the study also acknowledges certain limitations. The use of abrasive materials during sample preparation, particularly with grits of 220 and 400, can result in the removal of surface crystals, potentially compromising data accuracy and the mineral rec-ord. To enhance the precision of results, we recommend avoiding such abrasives in future studies and exploring alternative preparation techniques that minimize crystal loss.

Another key limitation involves the low resolution along the z-axis during 3D reconstruction, which can lead to significant information loss regarding the three-dimensional shape of garnets. To address this, it is essential to carefully evaluate acquisition parameters, such as voxel size and scanning area, during the imaging process to improve the precision of data interpretation.

Looking ahead, this study lays a strong foundation for future research in petrology and geology. We recommend that future investigations apply this methodology to other geological contexts, which could yield new insights into mineral formation processes and metamorphic evolution. Further exploration of alternative preparation methods and improvements in 3D reconstruction techniques are crucial for enhancing data accuracy. Finally, the integration of advanced imaging techniques, such as infrared digital holography, could provide real-time insights into crystallization and growth dynamics, offering even greater detail about the internal structure and deformation mechanisms of garnets.

This work provides valuable insights into garnet nucleation and growth processes, setting the stage for further exploration and a more comprehensive understanding of metamorphic rock evolution and mineral formation.

Acknowledgments

This research forms part of the undergraduate thesis of L.M. Hernandez. We are indebted to the Universidad Industrial de Santander for their support in the availability of its analytical facilities (Laboratory of Microscopy) and their professional staff for helpful comments, discussion, and assistance with the analytical data acquisition. The authors also acknowledge to the anonymous reviewers for their critical and insightful

reading of the manuscript and are most grateful to the above-named people and institutions for support.

References

[1] Marsh, B.D. On the Interpretation of Crystal Size Distributions in Magmatic Systems. J. Petrol. 39 (1998) 553-599.

[2] Proussevitch, A.A., Sahagian, D.L., Carlson, W.D. Statistical analysis of bubble and crystal size distributions: Application to Colorado Plateau basalts. J. Volcanol. Geotherm. Res. 164 (2007) 112-126.

[3] Jerram, D.A., Higgins, M. 3D analysis of rock textures: quantifying igneous microstructures. Elements 3 (2007) 239-245.

[4] Jerram, D.A., Mock, A., Davis, G.R., Field, M., Brown, R.J. 3D crystal size distributions: A case study on quantifying olivine populations in kimberlites. Lithos 112 (2009) 223-235.

[5] Brugger, C.R., Hammer, J.E. Crystal size distribution analysis of plagioclase in experimentally decompressed hydrous rhyodacite magma. Earth Planet. Sci. Lett. 300 (2010) 246–254.

[6] Berger, A., Herwegh, M., Schwarz, J.-O., Putlitz, B. Quantitative analysis of crystal/grain sizes and their distributions in 2D and 3D. J. Struct. Geol. 33 (2011) 1751-1763.

[7] Chen, S.-S., Wang, J.-C. Magmatic processes in the Comei large igneous province: Insights from quantitative plagioclase composition and texture analysis. J. Volcanol. Geotherm. Res. (2026) 108559.

[8] Chen, Y., Tang, D., Xu, H., Tao, Sh., Li, S., Yang, G., Yu, J. Pore and fracture characteristics of different rank coals in the eastern margin of the Ordos Basin, China. J. Nat. Gas Sci. Eng. 26 (2015) 1264-1277.

[9] Mayo, Sh., Josh, M., Nesterets, Y., Esteban, L., Pervukhina, M., Ben Clennell, M., Maksimenko, A., Hall, Ch. Quantitative micro-porosity characterization using synchrotron micro-CT and xenon K-edge subtraction in sandstones, carbonates, shales and coal. Fuel 154 (2015) 167-173.

[10] Voorn, M., Exner, U., Barnhoorn, A., Baud, P., Reuschlé, T. Porosity, permeability and 3D fracture network characterisation of dolomite reservoir rock samples. J. Petrol. Sci. Eng. 127 (2015) 270-285.

[11] Teles, A.P., Lima, I., Lopes, R.T. Rock porosity quantification by dual-energy X-ray computed microtomography. Micron 83 (2016) 72-78.

[12] Higgins, M.D. Quantitative Textural Measurements in Igneous and Metamorphic Petrology. Cambridge University Press, Cambridge, UK, 2006. 276 pp.

[13] Marsh, B.D. Crystal size distribution (CSD) in rocks and the kinetics and dynamics of crystallization I. Theory. Contrib. Mineral. Petrol. 99 (1988) 277-291.

[14] Cashman, K.V., Ferry, J.M. Crystal size distribution (CSD) in rocks and the kinetics and dynamics of crystallisation. III. Metamorphic crystallisation. Contrib. Mineral. Petrol. 99 (1988) 401–415.

[15] Huang, H., Yuan, E., Zhang, D., Sun, D., Yang, M., Zheng, Z., Zhang, Z., Gao, L., Panezai, S., Qiu, K. Free field of view infrared digital holography for mineral crystallization. Cryst. Growth Des. 23 (2023) 7992-8008.

[16] Randolph, A., Larson, M. Theory of Particulate Processes, Academic Press, New York (1971).

[17] Microsoft. Microsoft Image Composite Editor 1.4.4 for Windows, Redmond, WA, USA. Available online: https://www.sevenforums.com/software/166653-microsoft-image-composite-editor-1-4-4-a.html (accessed on 23 November 2023).

[18] Terrell, E.J., Higgs, C.F. Hydrodynamics of slurry flow in chemical mechanical polishing a review. J. Electrochem. Soc. 153 (2006) 15-22.

[19] Liao, L., Xi, F.J., Liu, K. Adaptive control of pressure tracking for polishing process. Int. J. Manuf. Eng. 132 (2010) 1-12.

[20] Khan, G.S., Gubarev, M., Speegle, C., Ramsey, B. Computer controlled cylindrical polishing process for development of grazing incidence optics for the hard X-ray region. Proc. SPIE, vol. 7802 (2010) Aug.

[21] Gu, Y. Automated scanning electron microscope based mineral liberation analysis: an introduction to JKMRC/FEI mineral liberation analyser. J. Miner. Mater. Charact. Eng. 2 (2003) 33.

[22] Blackson, J., Todd, C.S., Bar, G., Reuschle, D., Janus, M., Darus, M., Nickles, A. Automated image acquisition at high spatial resolutions in a field emission gun scanning electron microscope. Microsc. Microanal. 14 (2008) 1210–1211.

[23] Buckman, J. Use of automated image acquisition and stitching in scanning electron microscopy: Imaging of large-scale areas of materials at high resolution. Microsc. Anal. 28 (2014) 13–15.

[24] Ogura, K., Yamada, M., Hirahara, O., Mita, M., Erdman, N., Nielsen, C. Gigantic montages with a fully automated FE-SEM (serial sections of a mouse brain tissue). Microsc. Microanal. 16 (2010) 52–53.

[25] Wójcicka, A., Wróbel, Z. The Panoramic Visualization of Metallic Materials in Macro- and Microstructure of Surface Analysis Using Microsoft Image Composite Editor (ICE). In: Information Technologies in Biomedicine. Ewa Piętka and Jacek Kawa, Eds. Springer Berlin Heidelberg, Berlin, Heidelberg (2012) 358–368.

[26] Vergès, J.M., Morales, J.I. The gigapixel image concept for graphic SEM documentation. Applications in archaeological use-wear studies. Micron 65 (2014) 15-19.

[27] Purswani, P., Karpyn, Z.T., Enab, K., Xue, Y., Huang, X. Evaluation of image segmentation techniques for image-based rock property estimation. J. Petrol. Sci. Eng. 195 (2020) 107890.

[28] Phan, J., Ruspini, L.C., Lindseth, F. Automatic segmentation tool for 3D digital rocks by deep learning. Sci. Rep. 11 (2021) 19123.

[29] Wang, Y.D., Shabaninejad, M., Armstrong, R.T., Mostaghimi, P. Deep neural networks for improving physical accuracy of 2D and 3D multi-mineral segmentation of rock micro-CT images. Appl. Soft Comput. 104 (2021) 107185.

[30] Liu, L., Yao, J., Imani, G., Sun, H., Zhang, L., Yang, Y., Zhang, K. Reconstruction of 3D multi-mineral shale digital rock from a 2D image based on multi-point statistics. Front. Earth Sci. 10 (2022) Article 1104401.

[31] Lee, M. Enhancing Multi-View 3D-Reconstruction Using Multi-Frame Super Resolution. PhD Thesis, University of Windsor, Canada, 2022.

[32] Ankegowda, S. Real time 3D object reconstruction using Multi-View Stereo (MVS) Networks. Eur. Chem. Bull. 12 (2024) 2550-2557.

[33] Jung, S., Lee, Y.-S., Lee, Y., Lee, K.T. 3D Reconstruction Using 3D Registration-Based ToF-Stereo Fusion. Sensors 22 (2022) 8369.

[34] Tahmasebi, P., Sahimi, M. Reconstruction of three-dimensional porous media using a single thin section. Phys. Rev. E 85 (2012) 066709.

[35] Xiong, Q., Baychev, T.G., Jivkov, A.P. Review of pore network modelling of porous media: Experimental characterisations, network constructions and applications to reactive transport. J. Contam. Hydrol. 192 (2016) 101-117.

[36] Fu, J., Xiao, D., Li, D., Thomas, H.R., Li, C. Stochastic reconstruction of 3D microstructures from 2D cross-sectional images using machine learning-based characterization. Comput. Methods Appl. Mech. Eng. 390 (2022) 114532.

[37] Chawla, N., Sidhu, R.S., Ganesh, V.V. Three-dimensional visualization and microstructure-based modeling of deformation in particle-reinforced composites. Acta Mater. 54 (2006) 1541-1548.

[38] Marschallinger, R. Correction of geometric errors associated with the 3-D reconstruction of geological materials by precision serial lapping. Mineral. Mag. 62 (1998) 783-792.

[39] Mock, A., Jerram, D.A. Crystal size distributions (CSD) in three dimensions: Insights from the 3D reconstruction of a highly porphyritic rhyolite. J. Petrol. 46 (2005) 1525-1541.

[40] Yang, J., Wright, J., Huang, T., Yi, M. Image super-resolution as sparse representation of raw image patches. In: Proceedings of the 2008 IEEE Conference on Computer Vision and Pattern Recognition (CVPR), IEEE, Anchorage, AK, USA (2008) 1-8.

[41] Herman, G.T. Fundamentals of Computerized Tomography: Image Reconstruction from Projection. Springer-Verlag: London, 2009.

[42] Andrä, H., Combaret, N., Dvorkin, J., Glatt, E., Han, J., Kabel, M., Keehm, Y., Krzikalla, F., Lee, M., Madonna, C., Marsh, M., Mukerji, T., Saenger, E.H., Sain, R., Saxena, N., Ricker, S., Wiegmann, A., Zhan, X. Digital rock physics benchmarks—Part I: Imaging and segmentation. Comput. Geosci. 50 (2013) 25-32.

[43] Tuller, M., Kulkarni, R., Fink, W. Segmentation of X-ray CT data of porous materials: A review of global and locally adaptive algorithms. In: Soil–water–root processes: Advances in tomography and imaging 61 (2013) 157-182.

[44] Zhu, Z., Wahid, K., Babyn, P., Cooper, D., Pratt, I., Carter, Y. Improved compressed sensing-based algorithm for sparse-view CT image reconstruction. Comput. Math. Methods Med. 2013 (2013) 185750.
[45] Garfi, G., John, C.M., Berg, S., Krevor, S. The sensitivity of estimates of multiphase fluid and solid properties of porous rocks to image processing. Transp. Porous Med. 131 (2020) 985-1005.
[46] Luzzati, F., Fasolo, A., Peretto, P. Combining Confocal Laser Scanning Microscopy with Serial Section Reconstruction in the Study of Adult Neurogenesis. Front. Neurosci. 5 (2011) 1-14.
[47] Patil, T., Mishra, S., Chaudhari, P., Khandale, S. Image stitching using Matlab. International J. Eng. Trends Technol. 4 (2013) 302-306.
[48] Khan, A.M., Ravi, S. Image Segmentation Methods: A Comparative Study. Int. J. Soft Comput. Eng. 3 (2013) 84-92.
[49] Shi, X., Misch, D., Vranjes-Wessely, S. A comprehensive assessment of image processing variability in pore structural investigations: Conventional thresholding vs. machine learning approaches. Gas Sci. Eng. 115 (2023) 205022.
[50] Kumar, I., Singh, A. Reconstruction of reservoir rock using attention-based convolutional recurrent neural network. Appl. Comput. Geosci. 24 (2024) 100202.
[51] Liu, J.T.C., Glaser, A.K., Bera, K., True, L.D., Reder, N.P., Eliceiri, K.W., Madabhushi, A. Harnessing non-destructive 3D pathology. Nat. Biomed. Eng. 5 (2021) 203–218.
[52] Bostanabad, R. Reconstruction of 3D microstructures from 2D images via transfer learning. Comput. Aided Des. 128 (2020) 102906.
[53] Tomasi, C., Manduchi, R. Bilateral filtering for gray and color images. In: Sixth International Conference on Computer Vision, IEEE, (1998) 839–846.
[54] Amiri, H., Vogel, H., Plümper, O. New 2D to 3D reconstruction of heterogeneous porous media via deep generative adversarial networks (GANs). J. Geophys. Res.: Machine Learn. Comput. 1 (2024) e2024JH000178.
[55] Waters, D.J., Lovegrove, D.P. Assessing the extent of disequilibrium and overstepping of prograde metamorphic reactions in metapelites from the Bushveld Complex aureole, South Africa. J. Metamorph. Geol. 20 (2002) 135-149.
[56] Higgins, M.D. Numerical Modelling of Crystal Shapes in thin sections: Estimation of Crystal habit and True Size. Am. Mineral. 79 (1994) 113–119.
[57] Higgins, M.D. Measurement of Crystal Size Distributions. Am. Mineral. 85 (2000) 1105-1116.
[58] Blundy, J., Cashman, K. Petrologic Reconstructions of Magmatic System variables and processes. Rev. Mineral. Geochem. 69 (2008) 179-239.
[59] Barker, A. Introduction to Metamorphic Textures and Microstructures Second edition. Stanley Thornes (Publishers) Ltd., 1998. 275p.
[60] Walther, J., Wood, B.J. Rate and mechanism in prograde metamorphism. Contrib. Mineral. Petrol. 88 (1984) 246-259.
[61] Ma, Z., Peng, L., Wang, J. Ultra-smooth polishing of high-precision optical surface. Optik 124 (2013) 6586-6589.
[62] Kadivar, M., Azarhoushang, B. Kinematics and material removal mechanisms of loose abrasive machining. En Tribology and Fundamentals of Abrasive Machining Processes (Third Edition) (pp. 507-536). Elsevier, 2022.
[63] Levin, D., Butz, B., Müller, E. Optimized Ar+-ion Milling Procedure for TEM Cross-Section Sample Preparation. Ultramicroscopy 111 (2011) 1636-1644.
[64] Żak, A., Łaszcz, A., Hasiak, M., Gerstein, G., Maier, H.J., Dudzinski, W. Ion polishing as a method of imaging the magnetic structures in CoNiGa monocrystal. Results Phys. 10 (2018) 277-280.
[65] Sammer, T., Shi, X., Khan, M.Z., Matkovic, A., Teichert, C., Raith, J.G. Influence of broad ion beam polishing on the surface roughness of hydrated cement paste and its implications on microstructural analysis. Cem. Concr. Res. 182 (2024) 107555.
[66] Díaz, M., Fernández, C. Characterization of tectono-metamorphic events using crystal size distribution (CSD) diagrams. A case study from the Acebuches metabasites (SW Spain). J. Struct. Geol. 25 (2003) 935–947.
[67] Peterson, T. A refined technique for measuring crystal size distributions in thin section. Contrib. Mineral. Petrol. 124 (1996) 395–405.
[68] Kretz, R. Kinetics of the crystallization of garnet at two localities near Yellowknife. Canad. Mineral. 12 (1973) 1-20.
[69] Galwey, A.K., Jones, K.A. An attempt to determine the mechanism of a natural mineral-forming reaction from examination of products. J. Chem. Soc. London (1963) 5681-5686.
[70] Voorhees, P.W. Ostwald Ripening of two-phase mixtures. Annu. Rev. Mater. Sci. 22 (1992) 197-215.
[71] Konrad-Schmolke, M., Handy, M.R., Babist, J., O'Brien, P.J. Thermodynamic modelling of diffusion-controlled garnet growth. Contrib. Mineral. Petrol. 16 (2005) 181–195.